



AIAA 2006-4957

**The Compressible Taylor Flow
in Slab Rocket Motors**

B. A. Maicke and J. Majdalani
Advanced Theoretical Research Center
University of Tennessee Space Institute
Tullahoma, TN 37388

Propulsion Conference and Exhibit

9–12 July 2006
Sacramento, CA

The Compressible Taylor Flow in Slab Rocket Motors

Brian A. Maicke* and Joseph Majdalani†

University of Tennessee Space Institute, Tullahoma, TN, 37388

In this paper, the compressible flow inside a rectangular, porous channel is considered. A Rayleigh-Janzen perturbation is applied to the inviscid, steady, two-dimensional, isentropic flow equations. Closed form expressions are derived for the main properties of interest. The results of the study are verified via numerical simulation, with laminar and turbulent models, and with available experimental data. The critical point where the flowfield reaches sonic conditions is determined analytically. Our analysis captures the steepening of the velocity profiles that has been reported in several studies using either computational or experimental methods. Finally, explicit design criteria are presented to quantify the effects of compressibility in rockets and other two-dimensional injection-driven chambers.

Nomenclature

a	chamber half height
a_0	speed of sound at the origin
L_0	chamber length
p	pressure normalized by reference value
T	temperature normalized by reference value
u	axial velocity normalized by a_0
v	radial velocity normalized by a_0

Subscripts and Symbols

0	reference condition at the origin
c	center-axis
s	sonic condition
-	dimensional quantity

I. Introduction

The development of flow models for practical problems follows an evolutionary process. First a simple model is developed and then as that basic problem is understood, more complex models are built by relaxing assumptions and including effects previously neglected. As each successive model is refined, the result becomes more suitable at mimicking experimental measurements. However, this increase in accuracy is not freely realized. The governing equations describing advanced models become more complex, the cost of solving them analytically or computationally increases, and it can be harder to extract physical meaning from their final expressions. For this reason, it is important to strike a balance between the required accuracy of an analysis and its complexity.

The flow of a fluid through a channel with permeable walls follows the same evolutionary pattern. Berman¹ first treats the incompressible flow through a permeable channel by perturbing a similarity solution for small wall injection or suction. Taylor² extends the idea of the permeable channel flow by using an integral method to describe the flow through not only rectangular channels, but also through tubes, cones, and wedges.

*Research Assistant, Department of Mechanical, Aerospace, and Biomedical Engineering. Student Member AIAA.

†Jack D. Whitfield Professor of High Speed Flows, Department of Mechanical, Aerospace, and Biomedical Engineering. Member AIAA.

Yuan³ considers Berman’s original work and seeks an asymptotic expansion valid for large injection Reynolds numbers. Each successive treatment extends both the scope and accuracy of the preceding analysis.

The study of the permeable walled channel has been used to approximate any number of a wide range of practical problems. Taylor’s groundbreaking work was inspired by the drying of paper in an automated paper mill. Berman was motivated to find how the porous channel could be used for filtration purposes. Yuan,⁴ and Peng and Yuan⁵ have studied the flow as a means to control temperature via sweat cooling. As for the present study, it is driven by a propulsion-related application. Ours shares the same objectives that led Culick,⁶ Traineau *et al.*,⁷ and Balakrishnan *et al.*⁸ to devise non-reactive formulations for the internal flowfield of a solid rocket motor.

Taylor’s analysis of the permeable walled channel gave a reliable approximation to the core flow inside a solid rocket motor. While the solution was inviscid, the normal injection condition secured at the injection surface enabled the fluid motion to retain some of the features one normally reserves for a viscous flow. To this date, Taylor’s incompressible model remains one of the most cited and utilized in solid rockets. It has been repeatedly considered by Traineau *et al.*,⁷ Apte and Yang,⁹ Najjar *et al.*,¹⁰ Balakrishnan *et al.*,¹¹ Beddini and Roberts,¹² and many others. The justification for its ubiquitous use stems from two key factors: the suitability of non-reactive models to simulate the harsh environment in a rocket motor and the validity of using a non-deformable permeable chamber with non-regressing walls. The first factor may be attributed to propellant heat release being confined to the relatively thin flame zone forming above the burning surface (Chu *et al.*¹³). The second factor may be associated with the weak sensitivity of the streamline curvature on the wall regression rate. As shown by Majdalani *et al.*¹⁴ the effects of propellant regression are small in the operational range of most motors.

The motivation for extending the solution to include compressibility has several reasons. While there have been studies that attempt to determine the effects of compressibility in solid rocket motors, none of these manage to capture the fully two-dimensional behavior in a closed form analysis. The most notable of these are analyses by Traineau *et al.*,⁷ King,¹⁵ Flandro,¹⁶ Balakrishnan *et al.*,⁸ and Gany and Aharon.¹⁷ Most are pseudo-one-dimensional or limited to numerical integral formulations; moreover, studies with analytical solutions often bear more severe limitations than those imposed in the present work. Evidently, if a compressible analog to the Taylor-Culick profile can be found, then such work would be valuable in terms of advancing the theory of internal, rotational, compressible flow. Secondly, with increases in computational power and complexity in available solvers, more accurate and extensive analytical models are becoming highly desirable to verify the efficacy of new computational methods. Just as an analytical solution by itself is of limited value without numerical confirmation, so do new computational codes require up-to-date analytical models for verification. Next, an improved compressible model can help improve the foundation of more elaborate analyses. A compressible steady flow model can help investigators to recast the time-dependent flow formulation in rocket motors; the existing relations represent waves that may be affected by compressibility effects (Majdalani¹⁸). Finally, a compressible Taylor representation could be applied to the nozzleless motor concept. As explained by Gany and Aharon,¹⁷ the nozzleless motor gains in simplicity what it lacks in power. The removal of the nozzle does lower the efficiency of the motor, but the cost savings gained from eliminating what can be a complex nozzle assembly may make the nozzleless motor an attractive, low cost alternative in some (ramboosting) applications.

The specific model of interest here is the steady, two-dimensional, inviscid, isentropic, compressible flow of a fluid through a rectangular channel with porous walls, using the method developed Majdalani.¹⁹ The practical application is toward the steady compressible flow of a solid rocket motor in a slab configuration.

II. Problem Definition

A. Geometry

To model the slab rocket, a rectangular chamber of length L_0 and half height of a is used. L_s is the sonic length and is specified as the distance from the origin that fluid in the rocket must travel to reach sonic conditions. The origin of the coordinate system describing the domain is located at the center of the headwall. The spatial variables x and y are defined as the directions parallel and normal to the center-axis. Taking advantage of symmetry, a solution can be obtained for the top half of the geometry, namely $0 \leq y \leq 1$ and $0 \leq x \leq L_0$, and mirrored across the center-axis.

Along the sidewalls of the rocket, a uniform injection velocity of U_w is imposed. While there are any number of factors that could affect the local velocity at the propellant surface, density fluctuations, localized

non-homogeneity of the propellant, and erosive burning to name a few, this constraint gives a reasonable approximation of the injection mechanism at the propellant surface. The headwall of the motor is solid and inert, giving a zero velocity boundary condition at the headwall.

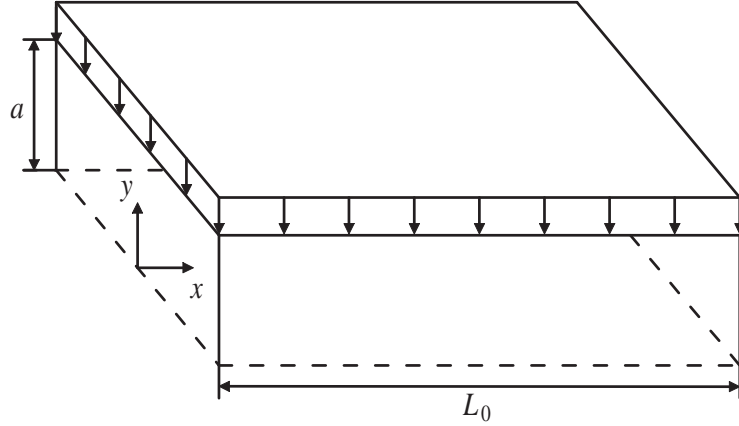


Figure 1. Porous channel with an inert headwall.

B. Non-dimensional Formulation

To facilitate the analysis, it is prudent to non-dimensionalize the variables of interest. A standard methodology is employed resulting in the following parameters:

$$u = \frac{\bar{u}}{a_0}; v = \frac{\bar{v}}{a_0}; p = \frac{\bar{p}}{p_0}; T = \frac{\bar{T}}{T_0}; \rho = \frac{\bar{\rho}}{\rho_0}; \psi = \frac{\bar{\psi}}{a_0 \rho_0 a}; \Omega = \frac{\bar{\Omega} a}{a_0}; \nabla = a \bar{\nabla} \quad (1)$$

These relations may be substituted back into the governing equations and boundary conditions to generalize the problem for all domains, rather than just one specific case.

The compressible stream function and the velocities are related through

$$u = \frac{1}{\rho} \frac{\partial \psi}{\partial y}; v = -\frac{1}{\rho} \frac{\partial \psi}{\partial x} \quad (2)$$

These relations are substituted into the vorticity definition to provide the first governing equation of interest.

$$\frac{\partial^2 \psi}{\partial x^2} + \frac{\partial^2 \psi}{\partial y^2} = \frac{1}{\rho} (\nabla \rho \cdot \nabla \psi) - \Omega \rho \quad (3)$$

In order to solve Eq. (3), another expression relating vorticity to the stream function is required for the right-hand-side of the equation to be fully determined. To that end, one may take the curl of the momentum equation to obtain the vorticity transport equation

$$\nabla \times (\mathbf{U} \times \boldsymbol{\Omega}) = \frac{1}{\gamma \rho^2} \nabla \rho \times \nabla p \quad (4)$$

The momentum equation may then be solved to determine the pressure from

$$\rho \nabla \left[\frac{1}{2 \rho^2} (\nabla \psi \cdot \nabla \psi) \right] + \Omega \nabla \psi = -\frac{\nabla p}{\gamma} \quad (5)$$

Finally, to bring closure to the thermodynamic variables, one may use

$$\rho = p^{\frac{1}{\gamma}}; T = p^{\frac{\gamma-1}{\gamma}} \quad (6)$$

Equation (6) is contingent on the flow being isentropic and calorically perfect.

Our boundary conditions stem from the physical determination of the system. For the rectangular solid rocket motor with an inert headwall, one may impose uniform injection at the sidewalls. Since the injection of the propellant at the sidewalls is normal to the surface, there is no axial flow at the wall. Symmetry provides yet another boundary condition. By allowing no flow to cross the line of symmetry, one may solve the equations for half of the chamber and then mirror the results. Finally, the headwall of the chamber is inert. Mathematically, these boundary conditions translate into

$$\bar{v}(\bar{x}, a) = -U_w; \bar{u}(\bar{x}, a) = 0; \bar{v}(\bar{x}, 0) = 0; \bar{u}(0, \bar{y}) = 0 \quad (7)$$

with the non-dimensional equivalents being

$$v(x, 1) = -M_w; u(x, 1) = 0; v(x, 0) = 0; u(0, y) = 0 \quad (8)$$

C. Perturbation Expansion

In order to solve Eqs. (3)-(6), a Rayleigh-Janzen perturbation may be applied. This requires expanding viz.

$$\begin{aligned} u(x, y) &= M_w u_0 + M_w^3 u_1 + O(M_w^5) & \rho(x, y) &= 1 + M_w^2 \rho_1 + M_w^4 \rho_2 + O(M_w^6) \\ v(x, y) &= M_w v_0 + M_w^3 v_1 + O(M_w^5) & p(x, y) &= 1 + M_w^2 p_1 + M_w^4 p_2 + O(M_w^6) \\ \psi(x, y) &= M_w \psi_0 + M_w^3 \psi_1 + O(M_w^5) & T(x, y) &= 1 + M_w^2 T_1 + M_w^4 T_2 + O(M_w^6) \\ \Omega(x, y) &= M_w \Omega_0 + M_w^3 \Omega_1 + O(M_w^5) \end{aligned} \quad (9)$$

The perturbation expansions from Eq. (9) may be substituted back into the governing equations, and then sorted by order of magnitude via standard perturbation methods. Substitution into Eq. (2) produces

$$O(M_w) : u_0 = \frac{\partial \psi_0}{\partial y}; O(M_w^3) : u_1 = \frac{\partial \psi_1}{\partial y} - \rho_1 \frac{\partial \psi_0}{\partial y} \quad (10)$$

The same approach may be applied to the crossflow velocity v to yield

$$O(M_w) : v_0 = -\frac{\partial \psi_0}{\partial x}; O(M_w^3) : v_1 = \rho_1 \frac{\partial \psi_0}{\partial x} - \frac{\partial \psi_1}{\partial x} \quad (11)$$

By substituting Eq. (1) into Eqs. (3)-(6) and segregating the leading-order terms, one obtains

$$O(M_w) : \frac{\partial^2 \psi_0}{\partial y^2} + \frac{\partial^2 \psi_0}{\partial x^2} = -\Omega_0 \quad (12)$$

$$O(M_w^2) : \nabla \times (\mathbf{U}_0 \times \Omega_0) = 0 \quad (13)$$

$$O(M_w^2) : -\frac{\nabla p_1}{\gamma} = \nabla \left(\frac{\nabla \psi_0 \cdot \nabla \psi_0}{2} \right) + \Omega_0 \nabla \psi_0 \quad (14)$$

$$O(M_w^2) : \rho_1 = \frac{p_1}{\gamma} \quad (15)$$

$$O(M_w^2) : T_1 = \frac{\gamma - 1}{\gamma} p_1 \quad (16)$$

Similarly, the leading-order expansion of the boundary conditions becomes

$$v_0(x, 1) = -1; u_0(x, 1) = 0; v_0(x, 0) = 0; u_0(0, y) = 0 \quad (17)$$

Since the governing equation that requires these boundary conditions is written in terms of the stream function, it is convenient to rewrite these using

$$\frac{\partial \psi_0(x, 1)}{\partial x} = 1; \frac{\partial \psi_0(x, 1)}{\partial y} = 0; \frac{\partial \psi_0(x, 0)}{\partial x} = 0; \frac{\partial \psi_0(0, y)}{\partial y} = 0 \quad (18)$$

The first-order governing equations may be obtained by collecting $O(M_w^3)$ and $O(M_w^4)$ terms of the expanded Eqs. (3)-(6); one extracts

$$O(M_w^3) : \frac{\partial^2 \psi_1}{\partial y^2} + \frac{\partial^2 \psi_1}{\partial x^2} = \nabla \rho_1 \cdot \nabla \psi_0 - \Omega_0 \rho_1 - \Omega_1 \quad (19)$$

$$O(M_w^4) : \nabla \times (\mathbf{U}_0 \times \boldsymbol{\Omega}_1) + \nabla \times (\mathbf{U}_1 \times \boldsymbol{\Omega}_0) = \nabla \rho_1 \times \nabla p_1 \quad (20)$$

$$O(M_w^4) : -\frac{\nabla p_2}{\gamma} = \nabla [(\nabla \psi_0 \cdot \nabla \psi_1) - \rho_1 (\nabla \psi_0 \cdot \nabla \psi_0)] + \rho_1 \nabla \left(\frac{\nabla \psi_0 \cdot \nabla \psi_0}{2} \right) + \Omega_0 \nabla \psi_1 + \Omega_1 \nabla \psi_0 \quad (21)$$

$$O(M_w^4) : \rho_2 = \frac{p_2}{\gamma} + \frac{1-\gamma}{\gamma} p_1^2 \quad (22)$$

$$O(M_w^4) : T_2 = \frac{\gamma-1}{\gamma} p_2 + \frac{1-\gamma}{2\gamma^2} p_1^2 \quad (23)$$

Since the boundary conditions must be satisfied by the leading-order equation, a set of homogeneous boundary conditions must be imposed from this point forward, specifically,

$$\begin{aligned} \rho_1 \frac{\partial \psi_0(x, 1)}{\partial x} - \frac{\partial \psi_1(x, 1)}{\partial x} &= 0; \quad \frac{\partial \psi_1(x, 1)}{\partial y} - \rho_1 \frac{\partial \psi_0(x, 1)}{\partial y} = 0 \\ \rho_1 \frac{\partial \psi_0(x, 0)}{\partial x} - \frac{\partial \psi_1(x, 0)}{\partial x} &= 0; \quad \frac{\partial \psi_1(0, y)}{\partial y} - \rho_1 \frac{\partial \psi_0(0, y)}{\partial y} = 0 \end{aligned} \quad (24)$$

III. Solution

A. Leading-Order Solution

In order to solve Eq. (12) one must determine an additional relationship between the vorticity and the stream function using the vorticity transport equation. Expanding Eq. (13) and substituting the stream function relations in place of velocity, one finds

$$\frac{\partial \psi_0}{\partial y} \frac{\partial \Omega_0}{\partial x} = \frac{\partial \psi_0}{\partial x} \frac{\partial \Omega_0}{\partial y} \quad (25)$$

Equation (25) will be satisfied when

$$\Omega_0 = C^2 \psi_0 \quad (26)$$

With Eq. (26) providing the crucial link between vorticity and the stream function, it is now possible to solve Eq. (12). The stream function may then be used to determine the leading-order quantities of all parameters of interest. It is interesting to note that because of the methodology chosen for this approach, namely the Rayleigh-Janzen perturbation expansion, the leading-order expansion should recover the incompressible solution to the slab rocket motor. With this in mind, Eq. (26) may be substituted into Eq. (12) such that

$$\frac{\partial^2 \psi_0}{\partial y^2} + \frac{\partial^2 \psi_0}{\partial x^2} + C^2 \psi_0 = 0 \quad (27)$$

This equation is easily separable with the outcome being

$$\psi_0 = (C_1 x + C_2) [C_3 \sin(Cy) + C_4 \cos(Cy)] \quad (28)$$

Straightforward application of the boundary conditions yields the leading-order term

$$\psi_0 = x \sin\left(\frac{1}{2}\pi y\right) \quad (29)$$

The determination of the first-order pressure is a simple process once the leading-order stream function is known. The first step is to remove the vorticity term from the equation by substituting the relation from Eq. (26). It is possible to further simplify the momentum equation by realizing that $\psi_0 \nabla \psi_0 = \frac{1}{2} \nabla \psi_0^2$. The result of these simplifications is an equation that may be integrated directly to determine the pressure. After some trigonometric simplifications, one finds

$$p_1 = -\frac{\gamma}{2} \left[\frac{1}{4} \pi^2 x^2 + \sin^2\left(\frac{1}{2}\pi y\right) \right] \quad (30)$$

Determining the first-order density and temperature is a trivial matter, requiring only the substitution of Eq. (30) into Eqs. (15) and (16), respectively. At the outset, one gets

$$\rho_1 = -\frac{1}{2} \left[\frac{1}{4} \pi^2 x^2 + \sin^2\left(\frac{1}{2}\pi y\right) \right]; \quad T_1 = \frac{1}{2}(1-\gamma) \left[\frac{1}{4} \pi^2 x^2 + \sin^2\left(\frac{1}{2}\pi y\right) \right] \quad (31)$$

B. First-Order Solution

The methodology for the first-order correction follows the same general outline as the leading-order analysis; one solves the vorticity transport equation, followed by the vorticity equation, the momentum equation for the pressure, and then finally the density and temperature from the isentropic relations. While this appears simple to implement, the first-order equations are more elaborate. It is not until the first-order corrections are determined, does one see the effects of compressibility on the internal flowfield of the slab rocket motor.

1. First-Order Vorticity Transport

As is the case in the leading-order analysis, the vorticity transport equation is used to determine the relationship between vorticity and the stream function at the first-order. To that end, Eq. (20) is examined to derive this relationship. The first simplification is realizing that p_1 and ρ_1 differ only by a constant, γ . The result of this is that the right-hand-side of Eq. (20) is zero since the evaluation of the cross product between two colinear vectors is zero. This simplifies the equation to

$$\nabla \times (\mathbf{U}_0 \times \boldsymbol{\Omega}_1) + \nabla \times (\mathbf{U}_1 \times \boldsymbol{\Omega}_0) = 0 \quad (32)$$

Vector operations may then be expanded into

$$\frac{\partial}{\partial x} (u_0 \Omega_1 + u_1 \Omega_0) + \frac{\partial}{\partial y} (v_0 \Omega_1 + v_1 \Omega_0) = 0 \quad (33)$$

To get the desired relationship between the first-order vorticity and the stream function, Eqs. (10), (11) and (26) are substituted. One obtains

$$\frac{\partial}{\partial x} \left[\frac{\partial \psi_0}{\partial y} \Omega_1 + \left(\frac{\partial \psi_1}{\partial y} - \rho_1 \frac{\partial \psi_0}{\partial y} \right) \frac{1}{4} \pi^2 \psi_0 \right] + \frac{\partial}{\partial y} \left[-\frac{\partial \psi_0}{\partial x} \Omega_1 + \left(\rho_1 \frac{\partial \psi_0}{\partial x} - \frac{\partial \psi_1}{\partial x} \right) \frac{1}{4} \pi^2 \psi_0 \right] = 0 \quad (34)$$

The derivatives are then evaluated and the expanded equation is simplified by canceling the proper terms to give

$$\frac{\partial \Omega_1}{\partial x} \frac{\partial \psi_0}{\partial y} - \frac{\partial \Omega_1}{\partial y} \frac{\partial \psi_0}{\partial x} = \frac{1}{4} \pi^2 \left[\psi_0 \left(\frac{\partial \rho_1}{\partial x} \frac{\partial \psi_0}{\partial y} - \frac{\partial \rho_1}{\partial y} \frac{\partial \psi_0}{\partial x} \right) + \frac{\partial \psi_1}{\partial x} \frac{\partial \psi_0}{\partial y} - \frac{\partial \psi_1}{\partial y} \frac{\partial \psi_0}{\partial x} \right] \quad (35)$$

At first glance this equation appears intractable. The method of determining a relation without fully solving the equation is not as practical for such a complex equation. However, further simplifications are possible if one realizes that the first-order vorticity is an extension of the leading-order term. It is not enough to set $\Omega_1 = \frac{1}{4} \pi^2 \psi_1$ as this expression does not satisfy Eq. (32). To find the proper expansion one must let

$$\Omega_1 = \frac{1}{4} \pi^2 \psi_1 + \Omega_c \quad (36)$$

where Ω_c is an additional correction. Equation (36) is then substituted back into Eq. (35) to provide

$$\frac{\partial \Omega_c}{\partial x} \frac{\partial \psi_0}{\partial y} - \frac{\partial \Omega_c}{\partial y} \frac{\partial \psi_0}{\partial x} = \frac{1}{4} \pi^2 \psi_0 \left(\frac{\partial \rho_1}{\partial x} \frac{\partial \psi_0}{\partial y} - \frac{\partial \rho_1}{\partial y} \frac{\partial \psi_0}{\partial x} \right) \quad (37)$$

whence

$$\Omega_c = \pm \frac{1}{32} \pi^2 x \left[\pi^2 x^2 \sin \left(\frac{1}{2} \pi y \right) + 4 \sin^2 \left(\frac{1}{2} \pi y \right) \right] + f(\psi_0) \quad (38)$$

and f is some function of ψ_0 . This function will be determined later to ensure that the first-order equation satisfies all of the requisite boundary conditions.

2. First-Order Vorticity

With the addition of Eq. (38), it is now possible to examine Eq. (19) as the equation is now fully defined in terms of known quantities and the first-order stream function. Substitution of Eqs. (26), (29), (31), and (38) into Eq. (19) gives

$$\begin{aligned}
\frac{\partial^2 \psi_1}{\partial y^2} + \frac{\partial^2 \psi_1}{\partial x^2} + \frac{1}{4} \pi^2 \psi_1 = & \\
-\nabla \left\{ \frac{1}{2} \left[\frac{1}{4} \pi^2 x^2 + \sin^2 \left(\frac{1}{2} \pi y \right) \right] \right\} \cdot \nabla \left[x \sin \left(\frac{1}{2} \pi y \right) \right] & \\
+ \frac{1}{8} \pi^2 \left[\frac{1}{4} \pi^2 x^2 + \sin^2 \left(\frac{1}{2} \pi y \right) \right] - \frac{1}{32} \pi^2 x \left[\pi^2 x^2 \sin \left(\frac{1}{2} \pi y \right) + 4 \sin^2 \left(\frac{1}{2} \pi y \right) \right] + f(\psi_0) &
\end{aligned} \tag{39}$$

After expansion of the vector operations and trigonometric simplification, one is left with

$$\frac{\partial^2 \psi_1}{\partial y^2} + \frac{\partial^2 \psi_1}{\partial x^2} + \frac{1}{4} \pi^2 \psi_1 = -\frac{1}{4} \pi^2 x \sin \left(\frac{1}{2} \pi y \right) \left[-\frac{1}{4} \pi^2 x^2 + 1 + \cos(\pi y) \right] - f(\psi_0) \tag{40}$$

It is possible to solve Eq.(40) by assuming an ansatz and then solving two coupled ordinary differential equations, rather than the single partial differential equation. After the work shown in the appendix, one retrieves

$$\psi_1 = -\frac{1}{48} x \sin \left(\frac{1}{2} \pi y \right) \{ \pi^2 x^2 [3 + \cos(\pi y)] + 3 [7 - \cos(\pi y)] \} \tag{41}$$

3. Second-Order Thermodynamic Variables

In order to determine the second-order pressure term, it is advantageous to expand the vector equation presented in Eq. (21) into two scalar equations:

$$\begin{aligned}
\frac{\partial p_2}{\partial x} = -\gamma \frac{\partial}{\partial x} \left\{ \frac{\partial \psi_0}{\partial x} \frac{\partial \psi_1}{\partial x} + \frac{\partial \psi_0}{\partial y} \frac{\partial \psi_1}{\partial y} - \rho_1 \left[\left(\frac{\partial \psi_0}{\partial x} \right)^2 + \left(\frac{\partial \psi_0}{\partial y} \right)^2 \right] \right\} & \\
+ \gamma \left\{ \frac{1}{2} \rho_1 \frac{\partial}{\partial x} \left[\left(\frac{\partial \psi_0}{\partial x} \right)^2 + \left(\frac{\partial \psi_0}{\partial y} \right)^2 \right] + \Omega_0 \frac{\partial \psi_1}{\partial x} + \Omega_1 \frac{\partial \psi_0}{\partial x} \right\} &
\end{aligned} \tag{42}$$

$$\begin{aligned}
\frac{\partial p_2}{\partial x} = -\gamma \frac{\partial}{\partial y} \left\{ \frac{\partial \psi_0}{\partial x} \frac{\partial \psi_1}{\partial x} + \frac{\partial \psi_0}{\partial y} \frac{\partial \psi_1}{\partial y} - \rho_1 \left[\left(\frac{\partial \psi_0}{\partial x} \right)^2 + \left(\frac{\partial \psi_0}{\partial y} \right)^2 \right] \right\} & \\
+ \gamma \left\{ \frac{1}{2} \rho_1 \frac{\partial}{\partial y} \left[\left(\frac{\partial \psi_0}{\partial x} \right)^2 + \left(\frac{\partial \psi_0}{\partial y} \right)^2 \right] + \Omega_0 \frac{\partial \psi_1}{\partial y} + \Omega_1 \frac{\partial \psi_0}{\partial y} \right\} &
\end{aligned} \tag{43}$$

Equations (42) and (43) may be directly integrated for

$$p_2 = -\frac{1}{384} \gamma \pi^4 x^4 + \frac{1}{128} \gamma \pi^2 x^2 (13 - \cos 2\pi y) + f(y) \tag{44}$$

$$p_2 = -\frac{1}{64} \gamma \pi^2 x^2 \cos^2 \pi y - \frac{1}{16} \gamma (\cos \pi y + \cos^2 \pi y) + f(x) \tag{45}$$

After examining the two solutions and applying the trigonometric identity, $\cos 2a = 2 \cos^2 a - 1$, it is possible to combine Eqs. (44) and (45) to determine the second-order pressure:

$$p_2 = -\frac{1}{384} \gamma \pi^4 x^4 + \frac{1}{64} \gamma \pi^2 x^2 (7 - \cos^2 \pi y) - \frac{1}{16} \gamma (\cos \pi y + \cos^2 \pi y) \tag{46}$$

Determining the second-order density is a matter of substituting the pressure terms from Eqs. (30) and (46) back into Eq. (22); one gets

$$\begin{aligned}
\rho_2 = \frac{1}{384} \pi^4 x^4 (2 - 3\gamma) & \\
+ \frac{1}{64} \pi^2 x^2 [9 - 2\gamma + 2(\gamma - 1) \cos \pi y - \cos^2 \pi y] + \frac{1}{32} [1 - \gamma + 2(\gamma - 2) \cos \pi y - (\gamma + 1) \cos^2 \pi y] &
\end{aligned} \tag{47}$$

Similarly the second-order temperature becomes

$$T_2 = \frac{1}{192} (1 - \gamma) [2\pi^4 x^4 - 3\pi^2 x^2 (5 + 2 \cos \pi y - \cos^2 \pi y) + 6(1 + 3 \cos^2 \pi y)] \quad (48)$$

after similar substitutions.

IV. Results and Discussion

A. Critical Length

In order to facilitate comparisons to past results both analytical and experimental, it is convenient to normalize the axial distance by the critical length of the motor. For ease of calculation, the maximum velocity will be used to calculate the critical length, as this will be the first point in the flow that reaches sonic conditions. The axial velocity and temperature at the center-axis may be written as

$$u_c = u(x, 0) = \frac{1}{2} M_w \pi x - \frac{1}{48} M_w^3 \pi x (9 - \pi^2 x^2) \quad (49)$$

$$T_c = T(x, 0) = 1 + \frac{1}{8} (\gamma - 1) M_w^2 \pi^2 x^2 - \frac{1}{96} (\gamma - 1) M_w^4 (12 - 9\pi^2 x^2 + \pi^4 x^4) \quad (50)$$

It is possible to determine the critical length of the motor to increasing degrees of accuracy by retaining more terms in the expressions for velocity and temperature. For a simple approximation of the choke length, the leading-order terms are retained to give the expression

$$\frac{1}{2} M_w \pi x = \sqrt{1 - \frac{1}{8} (\gamma - 1) M_w^2 \pi^2 x^2} \quad \text{or} \quad x_s = \frac{2\sqrt{2}}{M_w \pi \sqrt{\gamma + 1}} \quad (51)$$

To increase the precision in calculating the sonic length, one may retain the second-order velocity terms and put

$$\frac{1}{2} M_w \pi x - \frac{1}{96} M_w^3 \pi x (18 - 2\pi x^2) = \sqrt{1 - \frac{1}{8} (\gamma - 1) M_w^2 \pi^2 x^2} \quad (52)$$

With the addition of the second-order velocity on the left-hand-side of the equation, the solution becomes more complex. The complexity of the equation for the sonic length has gone up from a simple quadratic to a more complicated cubic equation. Solving Eq. (52) and selecting the real, positive root gives the following

$$x_s^{(1)} = \frac{1}{\pi M_w} \sqrt{\frac{9M_w^4 + 6M_w^2(\beta^{\frac{1}{3}} - 8) + \beta^{\frac{2}{3}} - 16\beta^{\frac{1}{3}} - 96\gamma + 160}{\beta^{\frac{1}{3}}}} \quad (53)$$

where β is

$$\beta = 32 \left[4(18\gamma - 5) + 9M_w^2(1 - 3\gamma) + 6\sqrt{2(9M_w^2(-4\gamma^2 - 3\gamma + 5) + 2(6\gamma^3 + 6\gamma^2 + 30\gamma - 25))} \right] \quad (54)$$

It is interesting to note that while the quantity under the radical in Eq. (53) is dependent on the Mach number, it is only weakly so. An approximate expression for the choke length may be written as

$$x_{sa}^{(1)} = \frac{1}{\pi M_w} \sqrt{\frac{\beta_a^{\frac{2}{3}} - 16\beta_a^{\frac{1}{3}} + 160 - 96\gamma}{\beta_a^{\frac{1}{3}}}} \quad (55)$$

where β_a is equal to

$$\beta_a = 128 \left(18\gamma - 5 + 3\sqrt{6\gamma^3 + 6\gamma^2 + 30\gamma - 25} \right) \quad (56)$$

The more compact, approximate expression for the choke length is accurate to three decimal places for the range of injection Mach numbers common to slab rocket motor applications.

Instead, one may retain all the terms of the expanded velocities and temperatures to recover an even more accurate expression of the choke length

$$\frac{1}{2}M_w\pi x - \frac{1}{96}M_w^3\pi x (18 - 2\pi x^2) = \sqrt{1 - \frac{1}{8}(\gamma - 1)M_w^2\pi^2 x^2 - \frac{1}{96}(\gamma - 1)M_w^4(12 - 9\pi^2 x^2 + \pi^4 x^4)} \quad (57)$$

The increase in complexity caused by retaining the final temperature term is not as noticeable as one might expect. The equation of interest remains a cubic equation, though with heavier coefficients. Equation (57) has the real, positive root

$$x_s^{(2)} = \frac{1}{\pi M_w} \sqrt{\frac{9M_w^4 + 6M_w^2 \left[\phi^{\frac{1}{3}} - 4(\gamma + 1) \right] + \phi^{\frac{2}{3}} - 8\phi^{\frac{1}{3}}(\gamma + 1) + 32(2\gamma^2 + \gamma - 1)}{\phi^{\frac{1}{3}}}} \quad (58)$$

where ϕ is

$$\begin{aligned} \phi = & -[36M_w^4(\gamma - 7) - 288M_w^2(\gamma^2 - \gamma - 2) + 128(4\gamma^3 + 3\gamma^2 - 6\gamma - 14)] \\ & + 12[-64M_w^4(11\gamma^4 + 85\gamma^3 + 63\gamma^2 - 76\gamma - 137) \\ & + 4608M_w^2(\gamma^4 + 2\gamma^3 + \gamma^2 - 3\gamma - 3) \\ & - 1024(3\gamma^4 + 14\gamma^3 + 6\gamma^2 - 18\gamma - 22)]^{\frac{1}{2}} \end{aligned} \quad (59)$$

Similar to the first-order equation, Eq. (58) is only weakly dependent on the Mach number; one finds a more manageable expression for the sonic length, namely,

$$x_{sa}^{(2)} = \frac{1}{\pi M_w} \sqrt{\frac{\phi_a^{\frac{2}{3}} - 8\phi_a^{\frac{1}{3}}(\gamma + 1) + 32(2\gamma^2 + \gamma - 1)}{\phi_a^{\frac{1}{3}}}} \quad (60)$$

where

$$\phi_a = -[128(4\gamma^3 + 3\gamma^2 - 6\gamma - 14)] + 12\sqrt{-1024(3\gamma^4 + 14\gamma^3 + 6\gamma^2 - 18\gamma - 22)} \quad (61)$$

as with the first-order approximation Eq. (60) is accurate to the third decimal place for most injection Mach numbers for rocket applications.

B. Computational Verification

In order to ensure that the perturbation expansion is valid, a numerical verification is provided. Version 6.1 of the Fluent computational fluid dynamics (CFD) solver provides the segregated, two-dimensional, double precision, compressible solver that will provide a basis for the numerical comparison. Laminar and Spalart-Allmaras models will all be used to account for the viscosity effects in the calculations. A rectangular geometry with a half height of 1 cm and a length of 45 cm is used to model the slab geometry. The solver provides data for the top half of the slab motor, which may then be mirrored across the center-axis. A uniform mass injection is imposed on the sidewalls of $13 \text{ kg m}^{-2} \text{ s}^{-1}$, providing a close approximation of the constant velocity injection used in the perturbation analysis. The injection gas is air with an injection temperature of 260 K, molecular weight of 29 kg kmol^{-1} , dynamic viscosity of $1.66 \times 10^{-5} \text{ kg m}^{-1} \text{ s}^{-1}$, and a ratio of specific heats of 1.4.

The first verification provided concerns the thermodynamic properties along the center-axis of the chamber, namely, the pressure and temperature. These parameters are chosen for their ease of calculation both numerically and analytically as well as for their ability to provide comparisons along the entire length of the simulated motor.

Figure 2(a) compares the center-axis pressure profile using $\gamma = 1.4$. All of the analytical and computational models agree at the headwall of the chamber. As the flow progresses through the chamber, the one-dimensional model over-predicts the center-axis pressure by a comfortable margin. Once reaching the aft end, the one-dimensional approximation steeply drops for a match to the numerically predicted value.

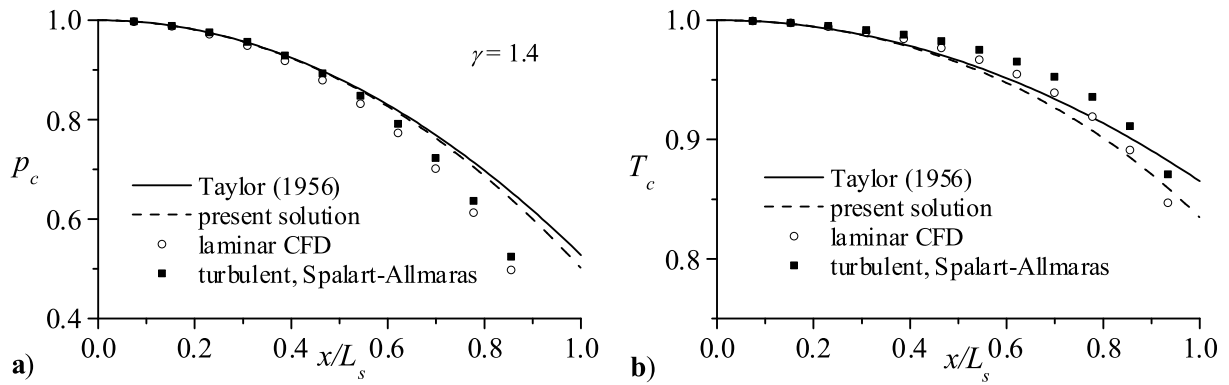


Figure 2. Comparison of the center-axis pressures and temperatures from analytical and computational models.

Examining the solution presented here, good agreement is observed at the headwall, with deviations from the numerical simulation appearing as the flow progresses to the aft end. It is interesting to note that the present solution more closely matches the Spalart-Allmaras model rather than the laminar flow model. This can be attributed to the quasi-viscous nature of the work, driven by the normal injection condition at the walls. Even though the solution is inviscid, it can approximate some features of viscous flow. Had a viscous model been used, one would have expected the deviation of pressures at the aft end to close even further.

The temperature comparison in Figure 2(b) presents a slightly different contrast. As in the pressure comparison, the agreement at the headwall of the chamber is excellent with deviations occurring as the flow progresses past the halfway point in the motor. The solution approaches the numerical models as the flow nears the exit of the motor. The present analysis more closely follows the laminar numerical model, rather than the more elaborate turbulent model. This is not unexpected and can be accounted for by two causes. The first is that while the normal injection condition at the walls provides a quasi-viscous behavior, it does not account for any thermal effects that a viscous flow may introduce. Thus, the present analytical model would be expected to under-predict the center-axis temperature. The second cause is that the energy model used to determine the temperature, namely isentropic flow, is restrictive. Relaxing the isentropic condition would no doubt lead to a more accurate prediction of the center-axis temperature.

It is also of interest to compare the predicted velocity profiles at various points in the motor chamber. Since high velocities can lead to changes in motor performance, it is important that these variations are correctly accounted for. In order to get good comparisons throughout the motor, comparisons are made for the center-axis velocities.

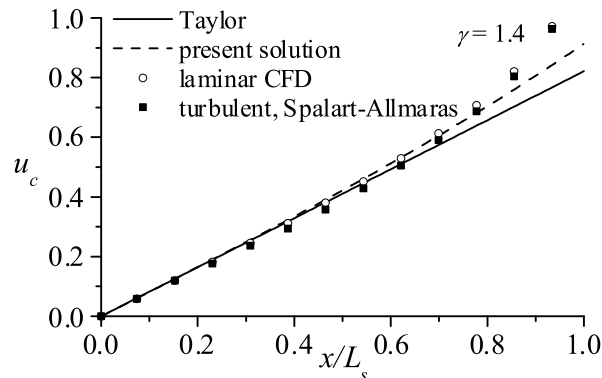


Figure 3. Comparison of predicted center-axis velocity with numerical results.

The center-axis comparison in Figure 3 shows some interesting features and generally good agreement with the numerical results. The present work matches well early in the chamber, but diverges under the

numerical predictions near the end of the chamber. This difference can be accounted for by the lack of viscous effects in our formulation. While it is true with the normal injection condition, some aspects of the solution may more closely approximate a viscous model, the effect of the normal injection decreases as the area of interest moves toward the center-axis. The result is a centerline flow with a slightly different shape than one accounting for viscosity. If the viscous losses were accounted for, no doubt the center-axis velocity would trend toward closer agreement with the numerical results.

C. Theoretical and Experimental Comparisons

Flow in a rectangular channel has been a topic studied in a number of different applications and as a result there is a wealth of theoretical and experimental data available to make comparisons against. Even in the relatively narrow application of the slab rocket motor, studies by Traineau *et. al.*⁷ and Gany and Aharon,¹⁷ provide both theoretical and experimental results. Taylor’s incompressible solution for the slab is also used as a benchmark.

The baseline for comparison is the pressure distribution at the center-axis of the motor. Traineau provides a one-dimensional, a pseudo-two-dimensional analysis using a stream tube analysis, and experimental data to compare against. The results here are somewhat surprising. The one dimensional model appears to closely match the experimental data for the center-axis pressure. Traineau notes the same, along with the justification for the two-dimensional numerical simulation to under-predict the experimental data. It is possible that the introduction of viscous effects would lower the axial gradient, thus explaining the two-dimensional results from Traineau being lower than the observed experimental data. However, it does not completely explain why the one dimensional model matches the center-axis pressure prediction so well, while being less accurate for other variables of interest. It is speculated that the effects of viscosity cancel in the one-dimensional model since the flow is injected along the center-axis. If this is the case, one would expect the relaxing of the inviscid condition to produce a shift down in the center-axis pressure, bringing the predicted pressure in line with experimental results.

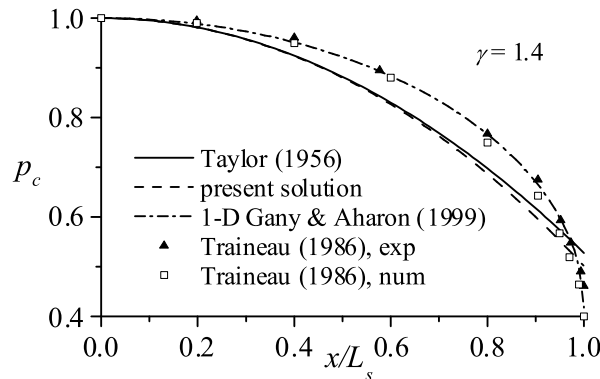


Figure 4. Comparison of center-axis pressures to former studies.

To assess compressibility effects on velocity profiles at varying locations in the motor, our solution will be paired with data from Traineau’s experimental and computational study. This enables us to not only see the evolution predicted by the present model, but gives a comparison grounded in reality with the experimental results. Traineau took measurements at various locations which, when normalized by the length of the motor, occur at approximately twenty percent increments of the total length beginning with forty percent.

The agreement of the asymptotic formulation with the experimental data shown in Figure 5 is encouraging. In all locations, the compressible model presented here more closely agrees with the experimental data than the incompressible model. Near the headwall of the motor both the incompressible and compressible models have close agreement with the experimental data, confirming that some length is required for the flow to develop to the point where compressibility effects become non negligible.

The axial velocity profiles evolve as the flow progresses through the motor. Near the headwall, the flow is nearly incompressible, following the sinusoidal profile predicted by Taylor. However, as the flow travels further down the motor, the velocity profile steepens. This steepening is found in both the experimental data and the computational verification of Traineau. It has been posited previously by Balakrishnan *et al.*⁸

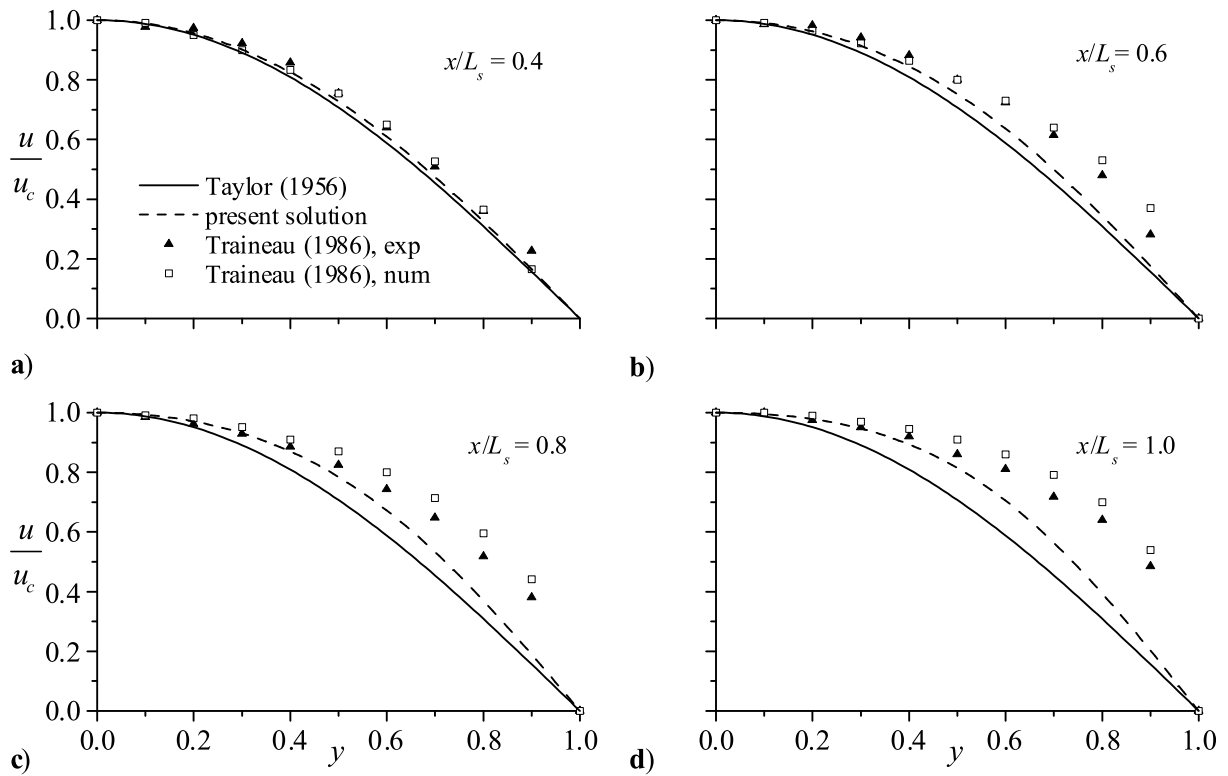


Figure 5. Comparison of the axial velocities at various motor locations.

that the steepening effects could be attributed to compressibility or turbulent viscous effects. Using the present model as a guide, one may see that at least a portion of the steepening effect can be attributed to correctly accounting for the effects of compressibility. While the agreement between the present model and the experimental data is not perfect, one would expect that properly accounting for viscosity and possible turbulent effects would further steepen the axial velocity profile, thus bringing it closer to agreement with the experimental measurements.

D. Streamlines

The behavior of the streamlines is illustrated by Figure 6. The solid lines depict the incompressible streamlines and the dotted lines show the effects of compressibility. When compressibility effects are accounted for, the streamlines turn more quickly, providing a steeper profile. As the injection velocity is increased, the behavior becomes more pronounced, and deviations from the incompressible condition are observed earlier in the flow. As the injection Mach number is increased, the motor length required for the flow to reach sonic conditions is decreased. This behavior is reflective of a strong correlation between the critical motor length and the injection Mach number as alluded to in Sec. A.

The streamline plots also show the effects of compressibility as the flow progresses through the motor. Near the headwall, the effects of compressibility are relatively negligible, a behavior that was previously observed in the numerical simulation. As the fluid travels toward the aft end and increases in speed, compressibility effects become more pronounced. Using the streamline plot as a guide, it is possible to calculate the point where the magnification of the velocity by compressibility becomes so large that it must be accounted for.

E. Compressible Design Criterion

This leads to an important question that every motor designer must ask: Do I need to worry about compressibility effects in my design or can I safely work with an incompressible model? In an attempt to answer

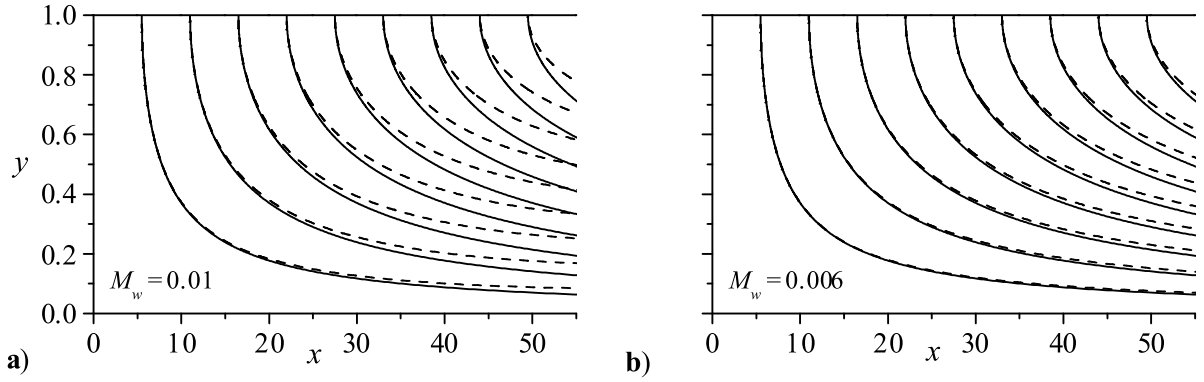


Figure 6. An illustration of the effects of compressibility on the streamlines of a slab rocket motor.

this question, one may look at a set of criteria for measuring the effects of compressibility. The first criterion is the compressibility ratio,

$$\chi_c = \frac{u(0, z)}{u_0(0, z)} \quad (62)$$

This is simply the ratio between the compressible and incompressible velocities. It represents the amplification of the center-axis velocity at a given location in the motor.

It is possible to obtain an analytical expression for the compressible amplification via substitution of Eqs. (9) and (10) back into Eq. (62). These yield

$$\chi_c = 1 + \frac{1}{24} M_w^2 (\pi^2 x^2 - 9) \quad (63)$$

One way for a motor designer to effectively make use of the formulation in Eq. (63) is to introduce an acceptable error, here labeled ϵ . If a designer knows that a velocity error of up to 5% is acceptable, he may let $\chi_c = 1 + \epsilon$. With this substitution and subsequent simplification, Eq. (63) becomes

$$x_\epsilon = \sqrt{\frac{24\epsilon}{M_w^2 \pi^2} + \frac{9}{\pi^2}} \quad (64)$$

This gives an expression for the location in the motor where an error of ϵ is first introduced. However for a designer looking to get a reasonable approximation, the $9/\pi^2$ may be ignored as the first term in the equation dominates for typical values expected in rocket design; one is left with

$$x_\epsilon = \frac{2\sqrt{6\epsilon}}{M_w \pi} \quad (65)$$

Conversely, if the geometry of the motor is fixed, the designer can get a rough approximation of the maximum injection Mach number by rearranging the equation to yield $2\sqrt{6\epsilon}/(\pi x)$. Since calculations of this type often degrade in the vicinity of the nozzle, it is common practice for a designer to specify that an error can be acceptable if it is limited to a small fraction of the motor length near the nozzle. To adjust for this, one may introduce $x = (1 - z)L$ where z is the fraction of the motor length where the error is acceptable (the last $\frac{1}{8}$ for example), and $L = L_0/a$ is the aspect ratio of the motor. This substitution yields

$$M_w^* = \frac{2\sqrt{6\epsilon}}{\pi(1 - z)L} \quad (66)$$

The validity of these criteria are easily verifiable. The compressibility criteria set forth in Eqs. (65) and (66) were used to select the stream function plots shown in Figure 6. This was accomplished by allowing a five percent deviation in the last eighth of the motor. In Figure 6(a), a designer would be well advised to absorb the extra complexity of the compressible model in favor of the more accurate flowfield prediction. Just from

a cursory examination of the streamlines, one may see significant deviations from the incompressible flow model almost immediately. In the second, less extreme case shown in Figure 6(b) the effects of compressibility are relatively negligible. Steepening of the streamlines is observed, but not in any degree that would alarm a potential designer.

V. Conclusion

The Rayleigh-Janzen perturbation approach presented here produces a compact, closed form solution with results in good agreement with both computation and experiment. The closed form expressions for the variables of interest help to further the understanding of compressibility effects on the flowfield of a solid rocket motor, where previously only numerical or experimental findings were available. Variations from the numerical analysis in pressure can be accounted for by the neglect of viscosity. The temperature is affected by the absence of viscosity and the isentropic assumption. Further analysis using a more complete energy model is suggested in an attempt to bring the temperature predictions to closer agreement with numerical values. In addition to advancement of compressible flow theory, practical relations are presented to aid the design of both regular and nozzleless rockets.

Appendix

Since $f(\psi_0)$ is used to satisfy the boundary conditions, it is expected that the $f(\psi_0)$ term will follow the form of the right-hand-side. To this end, one posits

$$f(\psi_0) = A_1 x \sin\left(\frac{1}{2}\pi y\right) + A_2 x^3 \sin^3\left(\frac{1}{2}\pi y\right) \quad (67)$$

to mirror the x terms in the right-hand-side. To further simplify bookkeeping one may let $\eta = \frac{1}{2}\pi y$. Next, a general solution is assumed

$$\psi_1(x, \eta) = xg(\eta) + x^3h(\eta) \quad (68)$$

Substitution of this back into Eq. (40) yields

$$\begin{aligned} & \frac{1}{4}\pi^2 [x(g'' + g) + x^3(h'' + h)] + 6xh = \\ & -\frac{1}{4}\pi^2 x \sin\left(\frac{1}{2}\pi y\right) \left[-\frac{1}{4}\pi^2 x^2 + 1 + \cos(\pi y)\right] + A_1 x \sin \eta + A_2 x^3 \sin^3 \eta \end{aligned} \quad (69)$$

where the primed quantities represent derivatives with respect to η . It is important to note that because of the change in variable, a $\pi^2/4$ constant multiplies the η derivative terms. Equation (69) simplifies by moving all terms to the left-hand-side and grouping them in powers of x . We gather

$$\begin{aligned} & x^3 \left[\frac{1}{4}\pi^2 \left(h'' + h - \frac{1}{4}\pi^2 \sin \eta \right) - A_1 \sin^3 \eta \right] \\ & + x \left[\frac{1}{4}\pi^2 (g'' + g + \sin \eta + \cos 2\eta \sin \eta) + 6h - A_2 \sin \eta \right] = 0 \end{aligned} \quad (70)$$

In order for Eq. (70) to be true for all values of x , the bracketed quantities multiplying both the x^3 and x terms must each be set to zero. The partial differential equation may thus be written as two ordinary differential equations.

$$h'' + h = \frac{1}{4}\pi^2 \sin \eta + A_1 \sin^3 \eta \quad (71)$$

$$g'' + g = \frac{4}{\pi^2} (A_2 \sin \eta - 6h) - \sin \eta - \cos 2\eta \sin \eta \quad (72)$$

Note that Eq. (71) is written only in terms of h , so that it can first be solved to determine h and then substituted into Eq. (72) to bring closure to the right-hand-side of that equation.

Solving Eq. (71) follows a similar procedure to that of the leading-order case. The only complication is that the equation is non-homogeneous, so a particular solution must be obtained in addition to a general

solution. Equation (71) becomes

$$\begin{aligned}
h &= C_1 \cos \eta + C_2 \sin \eta \\
&+ \frac{1}{16} \pi^2 (\cos \eta \sin 2\eta - 2\eta \cos \eta - \sin \eta - \cos 2\eta \sin \eta) \\
&+ \frac{A_1}{8\pi^2} (\cos 4\eta \sin \eta + 8 \cos \eta \sin 2\eta - 12\eta \cos \eta - 4 \cos 2\eta \sin \eta - \cos \eta \sin 4\eta)
\end{aligned} \tag{73}$$

This may then be substituted to the right-hand-side of Eq. (72) so that all of the non-homogeneous terms are determined. This follows the same methodology used to determine Eq. (73) with the differences from adjusting for the change in the non-homogeneous terms. One obtains

$$\begin{aligned}
g &= C_3 \cos \eta + C_4 \sin \eta \\
&+ \frac{A_1}{16\pi^4} [144 (\eta \cos \eta + \eta \cos \eta \cos 2\eta + \eta^2 \sin \eta + \eta \sin \eta \sin 2\eta) \\
&+ 156 \cos 2\eta \sin \eta - 132 \cos \eta \sin 2\eta + 6 (\cos 4\eta \sin \eta - \cos \eta \sin 4\eta)] \\
&+ \frac{A_2}{\pi^2} (\cos \eta \sin 2\eta - 2\eta \cos \eta - \cos 2\eta \sin \eta) \\
&- \frac{6C_1}{\pi^2} (\cos \eta \cos 2\eta + 2\eta \sin \eta + \sin \eta \sin 2\eta) \\
&+ \frac{6C_2}{\pi^2} (\cos 2\eta \sin \eta + 2\eta \cos \eta - \cos \eta \sin 2\eta) \\
&+ \frac{1}{16} [12 (\eta \cos \eta \cos 2\eta + \eta^2 \sin \eta + \eta \sin \eta \sin 2\eta) + 10 \cos 2\eta \sin \eta - \\
&6 \cos \eta \sin 2\eta + 4\eta \cos \eta + \cos 4\eta \sin \eta - \cos \eta \sin 4\eta]
\end{aligned} \tag{74}$$

Now the relationships for h and g may be substituted back into Eq. (68); one gets

$$\begin{aligned}
\psi_1 &= \frac{1}{16\pi^4} x (-2 \cos \eta \{12A_1\eta(\pi^2 x^2 - 12) \\
&+ \pi^2 [16A_2\eta + \pi^4 x^2 \eta + 48(C_1 - 2\eta C_2) - 8\pi^2(\eta + x^2 C_1 + C_3)]\} \\
&+ 4 \sin \eta \{3A_1[\pi^2 x^2 + 12(\eta^2 - 1)] + \pi^2 [4A_2 - 24(2\eta C_1 + C_2) \\
&+ \pi^2(-2 + 3\eta^2 + 4x^2 C_2 + 4C_4)]\} + \sin 3\eta [\pi^4 + 2A_1(\pi^2 x^2 + 3)])
\end{aligned} \tag{75}$$

While Eq. (75) does not appear to be the explicit expression that one hopes captures the effects of compressibility on the stream function, potential for simplification stems from administering the boundary conditions. Though appearing more involved, the solution for the undetermined coefficients follows the same agenda as the determination of the leading-order coefficients. One first examines the no flow across the center-axis from Eq. (24), recalling that it is evaluated at $(x, 0)$

$$-\frac{6C_1}{\pi^2} + C_3 + 3x^2 C_1 = 0 \tag{76}$$

In order for this equation to be true for all values of x the coefficients multiplying the x^2 and the x^0 terms must vanish independently. This single boundary condition may actually be used as two equations, namely

$$C_1 = 0 \quad \text{and} \quad C_3 = 0 \tag{77}$$

Revisiting Eq. (24), one has

$$\begin{aligned}
&\frac{1}{16\pi^4} x^3 \left(6A_1 \pi^4 + \frac{1}{2} \pi^8 \right) + \\
&\frac{1}{16\pi^4} x \left[-72A_1 \pi^2 + 8A_2 \pi^4 - 4\pi^6 + 4 \left(18A_1 \pi^2 + \frac{1}{2} 3\pi^6 \right) - 48\pi^4 C_2 \right] = 0
\end{aligned} \tag{78}$$

This is separated into two equations such that Eq. (78) holds for all values of x

$$A_1 = -\frac{1}{12} \pi^4 \quad \text{and} \quad 8A_2 \pi^4 + 2\pi^6 - 48\pi^4 C_2 = 0 \tag{79}$$

Leaving Eq. (79) momentarily, it is advantageous to apply the final boundary condition from Eq. (24)

$$x^2 \left(3C_2 - \frac{1}{32} \pi^2 \right) + C_4 + \frac{23}{32} + \frac{A_2}{\pi^2} - \frac{6C_2}{\pi^2} = 0 \quad (80)$$

which segregates into

$$C_2 = \frac{1}{96} \pi^2 \quad \text{and} \quad C_4 + \frac{21}{32} + \frac{A_2}{\pi^2} = 0 \quad (81)$$

and solving Eqs. (79) and (81) simultaneously determines the final two constants

$$A_2 = -\frac{3}{16} \pi^2 \quad \text{and} \quad C_4 = -\frac{15}{32} \quad (82)$$

Acknowledgments

This project is sponsored by the National Science Foundation through NSF Grant No. CMS-0353518 and, through matching funds, by the University of Tennessee Space Institute (UTSI).

References

- ¹Berman, A. S., "Laminar Flow in Channels with Porous Walls," *Journal of Applied Physics*, Vol. 24, No. 9, 1953, pp. 1232–1235.
- ²Taylor, G. I., "Fluid Flow in Regions Bounded by Porous Surfaces," *Proceedings of the Royal Society, London, Series A*, Vol. 234, No. 1199, 1956, pp. 456–475.
- ³Yuan, S. W., "Further Investigation of Laminar Flow in Channels with Porous Walls," *Journal of Applied Physics*, Vol. 27, No. 3, 1956, pp. 267–269.
- ⁴Yuan, S., *Turbulent Flows and Heat Transfer*, Vol. V, chap. "Cooling by Protective Fluid Films", Princeton University Press, Princeton, New Jersey, 1959, Section G.
- ⁵Peng, Y. and Yuan, S. W., "Laminar Pipe Flow with Mass Transfer Cooling," *Journal of Heat Transfer*, Vol. 87, No. 9, 1965, pp. 252–258.
- ⁶Culick, F. E. C., "Rotational Axisymmetric Mean Flow and Damping of Acoustic Waves in a Solid Propellant Rocket," *AIAA Journal*, Vol. 4, No. 8, 1966, pp. 1462–1464.
- ⁷Traineau, J.-C., Hervat, P., and Kuentamann, P., "Cold-Flow Simulation of a Two-Dimensional Nozzleless Solid Rocket Motor," *AIAA Joint Propulsion Conference*, No. 86-1447, Huntsville, Alabama, June 1986.
- ⁸Balakrishnan, G., Linan, A., and Williams, F. A., "Rotational Inviscid Flow in Laterally Burning Solid Propellant Rocket Motors," *Journal of Propulsion and Power*, Vol. 8, No. 6, 1992, pp. 1167–1176.
- ⁹Apte, S. and Yang, V., "Unsteady Flow Evolution in a Porous Chamber with Surface Mass Injection. Part I: Free oscillation," *AIAA Journal*, Vol. 39, No. 8, 2001, pp. 1577–1586.
- ¹⁰Najjar, F. M., Haselbacher, A., Ferry, J. P., Wasistho, B., Balachandar, S., and Moser, R., "Large-scale Multiphase Large-eddy Simulation of Flows in Solid-rocket Motors," *AIAA Computational Fluid Dynamics Conference*, No. 2003-3700, Orlando, FL, June 2003.
- ¹¹Balakrishnan, G., Linan, A., and Williams, F. A., "Compressible Effects in Thin Channels with Injection," *AIAA Journal*, Vol. 29, No. 12, 1991, pp. 2149–2154.
- ¹²Beddini, R. A. and Roberts, T. A., "Response of Propellant Combustion to a Turbulent Acoustic Boundary Layer," *Journal of Propulsion and Power*, Vol. 8, No. 2, 1992, pp. 290–296.
- ¹³Chu, W. W., Yang, V., and Majdalani, J., "Premixed Flame Response to Acoustic Waves in a Porous-walled Chamber with Surface Mass Injection," *Combustion and Flame*, Vol. 133, No. 6129, 2003, pp. 359–370.
- ¹⁴Majdalani, J., Vyas, A. B., and Flandro, G. A., "Higher Mean-flow Approximation for a Solid Rocket Motor with Radially Regressing Walls," *AIAA Journal*, Vol. 40, No. 9, September 2002, pp. 1780–1788.
- ¹⁵King, M. K., "Consideration of Two-dimensional Flow Effects on Nozzleless Rocket Performance," *Journal of Propulsion and Power*, Vol. 3, No. 3, 1987, pp. 194–195.
- ¹⁶Flandro, G. A., "Stability Prediction for Solid Propellant Rocket Motors with High-Speed Mean Flow," Final Technical AFRPL-TR-79-98, Air Force Rocket Propulsion Laboratory, Edwards AFB, CA, August 1980.
- ¹⁷Gany, A. and Aharon, I., "Internal Ballistics Considerations of Nozzleless Rocket Motors," *Journal of Propulsion and Power*, Vol. 15, No. 6, 1999, pp. 866–873.
- ¹⁸Majdalani, J., "The Oscillatory Channel Flow with Arbitrary Wall Injection," *Journal of Applied Mathematics and Physics*, Vol. 52, No. 1, 2001, pp. 33–61.
- ¹⁹Majdalani, J., "The Compressible Taylor-Culick Flow," *AIAA Joint Propulsion Conference*, No. 2005-3542, Tuscon, AZ, 2005.